# Interstitial solute transport in 3D reconstructed neuropil occurs by diffusion rather than bulk flow

Karl Erik Holter[a,b], Benjamin Kehlet[a,b], Anna Devor[c,d,e], Terrence J. Sejnowski[f,g], Anders M. Dale[d,e], Stig W. Omholt[h], Ole Petter Ottersen[i,1], Erlend Arnulf Nagelhus[j], Kent-André Mardal[b,k], and Klas H. Pettersen[j,2]

[a]Department of Informatics, University of Oslo, 0316 Oslo, Norway; [b]Center for Biomedical Computing, Simula Research Laboratory, N-1325 Lysaker, Norway; [c]Athinoula A. Martinos Center for Biomedical Imaging, Massachusetts General Hospital, Charlestown, MA 02129; [d]Department of Neurosciences, University of California, San Diego, La Jolla, CA 92093; [e]Department of Radiology, University of California, San Diego, La Jolla, CA 92093; [f]Howard Hughes Medical Institute, The Salk Institute for Biological Studies, La Jolla, CA 92037; [g]Division of Biological Sciences, University of California, San Diego, La Jolla, CA 92093; [h]Department of Circulation and Medical Imaging, Cardiac Exercise Research Group, Norwegian University of Science and Technology (NTNU), 7491, Trondheim, Norway; [i]Division of Anatomy, Department of Molecular Medicine, Institute of Basic Medical Sciences, University of Oslo, 0317 Oslo, Norway; [j]GliaLab and Letten Centre, Division of Physiology, Department of Molecular Medicine, Institute of Basic Medical Sciences, University of Oslo, 0317 Oslo, Norway; and [k]Department of Mathematics, University of Oslo, 0316 Oslo, Norway

Edited by Jennifer Lippincott-Schwartz, Howard Hughes Medical Institute, Ashburn, VA, and approved July 25, 2017 (received for review April 26, 2017)

**The brain lacks lymph vessels and must rely on other mechanisms for clearance of waste products, including amyloid $\beta$ that may form pathological aggregates if not effectively cleared. It has been proposed that flow of interstitial fluid through the brain's interstitial space provides a mechanism for waste clearance. Here we compute the permeability and simulate pressure-mediated bulk flow through 3D electron microscope (EM) reconstructions of interstitial space. The space was divided into sheets (i.e., space between two parallel membranes) and tunnels (where three or more membranes meet). Simulation results indicate that even for larger extracellular volume fractions than what is reported for sleep and for geometries with a high tunnel volume fraction, the permeability was too low to allow for any substantial bulk flow at physiological hydrostatic pressure gradients. For two different geometries with the same extracellular volume fraction the geometry with the most tunnel volume had 36% higher permeability, but the bulk flow was still insignificant. These simulation results suggest that even large molecule solutes would be more easily cleared from the brain interstitium by diffusion than by bulk flow. Thus, diffusion within the interstitial space combined with advection along vessels is likely to substitute for the lymphatic drainage system in other organs.**

glymphatic | interstitial fluid | extracellular space | simulation | AQP4

Transport of nutrients and waste within the brain's parenchyma is paramount to healthy brain function.

Although lymphatic vessels occur within the meninges (1, 2), they are absent from the brain's parenchyma. This raises the question of how waste products are cleared from the brain (3–8). There is an urgent need to resolve this question, given the fact that several neurological disorders are associated with accumulation of toxic debris and molecules in the brain interstitium (9). Most notably, insufficient clearance may contribute to the development of Alzheimer's disease and multiple sclerosis (9, 10).

Recently the "glymphatic" hypothesis (10) was launched. This hypothesis holds that the brain is endowed with a waste clearance system driven by bulk flow of fluid through the interstitium, from paraarterial to paravenous spaces, facilitated by astrocytic aquaporin-4 (AQP4). Further, it was proposed that cerebral arterial pulsation (11) and respiration (12) drive paravascular fluid movement and cerebrospinal fluid (CSF)–interstitial fluid (ISF) exchange. Here, bulk flow is defined as the movement of fluid down the pressure gradient, advection is the transport of a substance by bulk flow, and convection is transport by a combination of advection and diffusion.

There is strong evidence for paravascular advection (8, 13–15), although the details of influx and efflux pathways and the underlying driving forces are debated (10, 15–17). There are, however, controversies regarding the relative importance of advective versus diffusive transport within the interstitial space (3, 5, 7, 8), and the idea that a hydrostatic pressure gradient can cause an advective flow within the interstitium has been questioned (3, 5, 6).

The recent generation of 3D reconstructions of brain neuropil together with representative extracellular space volume estimates have now finally opened the pathway for realistic simulations of solute transport in brain. Although the convoluted and very fine structure of the interstitial space makes such simulations challenging, we were able to simulate the flow and estimate the permeability for EM reconstructions from Kinney et al. (18) by meshing the interstitial space into almost 100 million tetrahedrons and describing the relevant physics in each tetrahedron by differential equations.

By simulating bulk flow in two versions of the EM reconstruction we find that the permeability is too low to allow for any substantial bulk flow for realistic hydrostatic pressure gradients. The results imply that diffusion prevails. Besides advancing understanding of waste clearance in brain, our results also elucidate how drugs distribute within brain neuropil after having permeated the blood–brain barrier.

## Significance

**Transport of nutrients and clearance of waste products are prerequisites for healthy brain function. It is still debated whether solutes are transported through the interstitial space by pressure-mediated bulk flow or by diffusion. Here we have simulated interstitial bulk flow within 3D electron microscope reconstructions of hippocampal tissue. We show that the permeability is one to two orders of magnitude lower than values typically seen in the literature, arguing against bulk flow as the dominant transport mechanism. Further, we show that solutes of all sizes are more easily transported through the interstitium by diffusion than by bulk flow. We conclude that clearance of waste products from the brain is largely based on diffusion of solutes through the interstitial space.**

Author contributions: K.E.H., B.K., A.D., T.J.S., A.M.D., S.W.O., O.P.O., E.A.N., K.-A.M., and K.H.P. designed research; K.E.H., K.-A.M., and K.H.P. performed research; and K.E.H., A.D., T.J.S., A.M.D., S.W.O., O.P.O., E.A.N., K.-A.M., and K.H.P. wrote the paper.

The authors declare no conflict of interest.

This article is a PNAS Direct Submission.

Freely available online through the PNAS open access option.

[1]Present address: Vice-Chancellor's Office, Aula Medica, Karolinska Institutet, 171 77 Stockholm, Sweden.

[2]To whom correspondence should be addressed. Email: klas.pettersen@gmail.com.

This article contains supporting information online at www.pnas.org/lookup/suppl/doi:10.1073/pnas.1706942114/-/DCSupplemental.

## Results

We used publicly available reconstructions (18) to simulate bulk flow through the interstitial space. The reconstructions were based on electron microscopy of serial sections of rat CA1 hippocampal neuropil. To correct for the volume changes known to occur during tissue preparation and embedding, Kinney et al. (18) adjusted the interstitial volume fraction from 8% in the original EM reconstruction to more physiologically realistic volume fractions of about 20% (19).

Kinney et al. (18) grouped the interstitial volume into tunnels or sheets. Sheets are the volumes between two adjacent membranes, typically 10–40 nm wide, and tunnels are the wider, interconnected structures found at the junction of three or more cells, about 40–80 nm wide. In Fig. 1*A* tunnels are colored in cyan and sheets in red. Kinney et al. (18) used different volume scaling procedures, some adding volume mainly to the tunnels and some adding volume to the sheets. We simulated interstitial bulk flow and computed the permeabilities from two different realizations of the EM reconstruction, both having approximately the same total interstitial volume fraction, but with different relative tunnel volume fractions. We also simulated bulk flow and permeability for smaller subvolumes with interstitial volume fractions up to 32.1%.

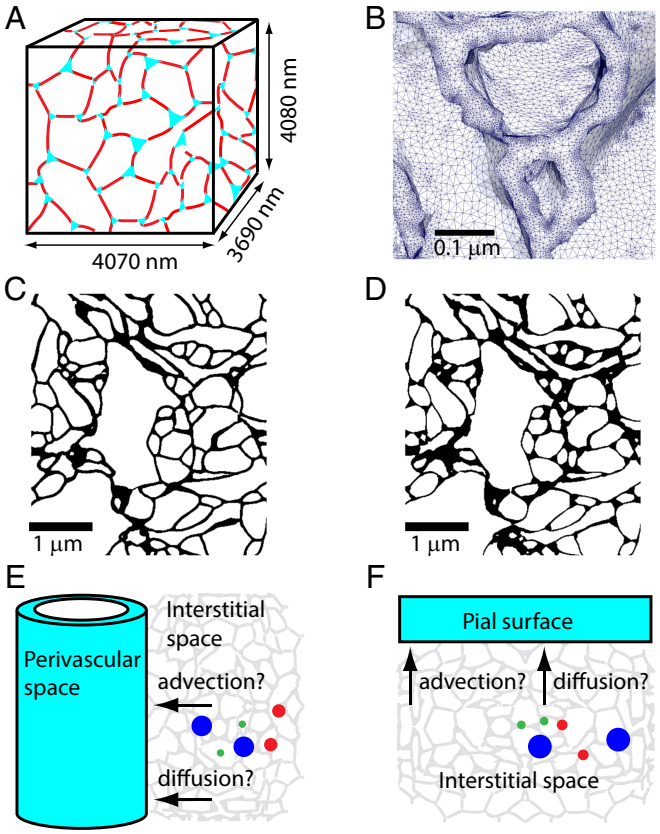


**Fig. 1.** Model systems and microscopic structure of the extracellular volume. (*A*) Schematic illustration of the EM reconstruction. Tunnels are in cyan and sheets in red. (*B*) Submicrometer partition of the EM reconstruction showing typical sizes of the 84 million tetrahedrons used in the simulation. (*C* and *D*) EM reconstruction from Kinney et al. (18) with a small tunnel volume fraction (*C*) and with a larger tunnel volume fraction (*D*). Both *C* and *D* have extracellular volume fractions of about 20% (20.1% and 20.7%, respectively). (*E*) Schematic illustration showing the cylinder model of the paravascular space and solutes (solid circles) in the surrounding interstitial space. (*F*) Schematic illustration showing the pial surface model.

Example sections from the two realizations are shown in Fig. 1 *C* and *D*, where Fig. 1*C* has the smallest relative tunnel fraction (33%), and Fig. 1*D* has the largest (63%). As described in *Methods*, the two tissue realizations were divided into 84 million and 25 million tetrahedrons, respectively, the smallest tetrahedrons with sides less than 1 nm (Fig. 1*B*). The flow and permeability were estimated by solving the Stokes equations in the FEniCS simulator (20) for a pressure gradient of 1 mmHg/mm applied between opposite sides of the tissue cube, assuming nonelastic and impermeable obstacles. The pressure gradient of 1 mmHg/mm is considered an absolute upper estimate of the assumed pressure gradient within brain tissue (*Discussion*), and the flow velocities and Péclet numbers shown here should therefore be considered upper estimates. Note that there is a linear relationship between pressure gradient and flow velocity, implying that a pressure gradient different from the 1 mmHg/mm used here will change the velocities with the same factor. In contrast, the estimated permeabilities will be preserved.

Based on the estimated permeabilities from the EM reconstructions we created two simplified model systems to compare the effect of solute clearance by diffusion versus advection. In Fig. 1 *E* and *F*, schematic illustrations of the two models are shown. Fig. 1*E* illustrates clearance toward the paravascular space, and Fig. 1*F* illustrates clearance toward the pial surface. Three solutes with different diffusion constants were studied, the smallest corresponding to the effective diffusion coefficient of potassium ions [$D^* = 77 \times 10^{-7}$ cm$^2$/s (21)], the medium sized corresponding to 3 kDa Texas Red Dextran [$D^* = 5.3 \times 10^{-7}$ cm$^2$/s (19)], and the largest having a diffusion constant corresponding to 70 kDa Dextran [$D^* = 0.84 \times 10^{-7}$ cm$^2$/s (19)].

**Flow and Permeability in Reconstructed Neuropil.** The intrinsic hydrodynamic permeability, $\kappa$, is defined by Darcy's law, $q = -\frac{\kappa}{\mu}\nabla p$, which states that there is a proportionality between the flux, $q$ (discharge per unit area, with units of length per time), and the pressure gradient, $\nabla p$, with $\mu$ denoting the viscosity. For the geometry with the smallest tunnel fraction (Fig. 1*C*) we estimated the permeability to be 10.9 nm$^2$, 10.3 nm$^2$, and 11.0 nm$^2$ (mean 10.7 nm$^2$) along the three orthogonal axes perpendicular to the sides of the rectangular tissue cuboid. For the geometry with a larger tunnel fraction (Fig. 1*D*) the permeability was estimated to be 16.6 nm$^2$, 14.4 nm$^2$, and 13.1 nm$^2$ (mean 14.7 nm$^2$) along the three orthogonal axes. Thus, the anisotropy was maximum 6% for the geometry with a low tunnel fraction and maximum 26% for the geometry with a high tunnel fraction.

The geometry with a high tunnel fraction had a 36% higher mean permeability than the geometry with a lower tunnel fraction (18), even though the extracellular volume fraction was approximately the same. The maximal velocities in Fig. 2 *A–C* are substantially lower than the maximal velocities in Fig. 2 *D–F*, where the former corresponds to the geometry with a low tunnel fraction and the latter corresponds to the geometry with a higher tunnel fraction. Further, the cross-sections show that the velocities are highest within the centers of the larger tunnels (Fig. 2 *A* and *D*). For all plots we have assumed a pressure gradient of 1 mmHg/mm. This assumption should be considered an upper estimate (*Discussion*). The average extracellular velocities are 8.95 nm/s and 12.2 nm/s, corresponding to permeabilities of 10.7 nm$^2$ and 14.7 nm$^2$, respectively. Note, however, that our convergence tests (*Methods*) revealed that the permeabilities and velocities may have been underestimated by as much as 30%. Thus, an upper estimate of the permeabilities would be 14 nm$^2$ and 19 nm$^2$, with corresponding mean velocities of 12 nm/s and 16 nm/s, respectively.

For both geometries it takes several hundred minutes before 50% of the fluid has traveled more than 100 μm (Fig. 2 *C* and

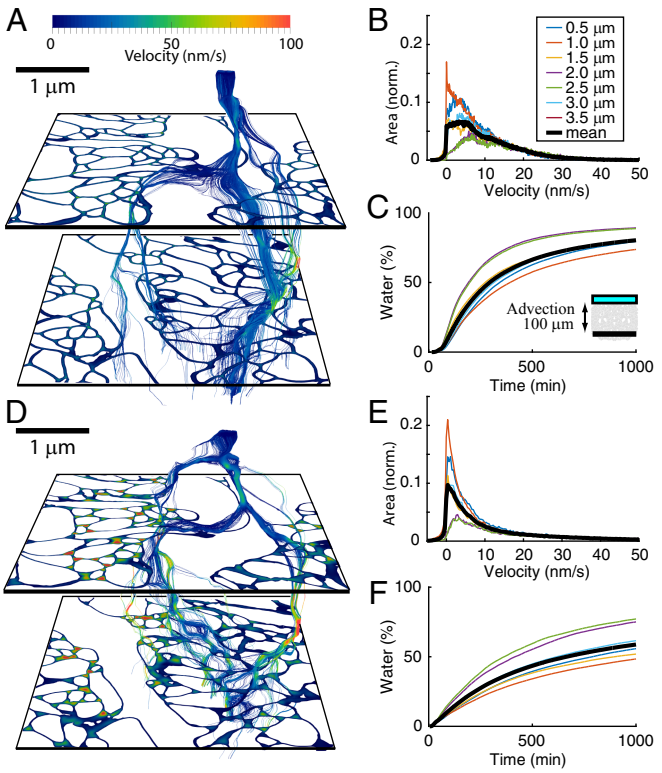


**Fig. 2.** Bulk flow velocity through the EM reconstruction from Kinney et al. (18). A pressure gradient of 1 mmHg/mm is applied in the vertical ($z$) direction. (*A*) The geometry with a low tunnel volume fraction. The cross-sections are at depth $z = 1.5$ μm and $z = 3.5$ μm. For clarity only streamlines originating from a small circle with radius 0.1 μm at $z = 0$ are shown. (*B*) Distribution of the $z$ component of flow velocities through different cross-sectional extracellular areas of the geometry in *A*, with the corresponding depth of the plane expressed in the key. All traces are normalized to the mean extracellular cross-sectional area. The mean distribution is shown in black. (*C*) The percentage of water which has reached 100 μm as a function of time (*Inset*), assuming each streamline to be straight, along the $z$ axis and with a constant velocity given by the velocity distribution in *B*. (*D–F*) Same as *A–C* for the EM reconstruction with a higher tunnel volume fraction, but approximately the same extracellular volume fraction.

*F*). For comparison, Xie et al. (22) show that 3 kDa Texas Red Dextran typically penetrated 100 μm in about 20 min in sleeping and in anesthetized mice, a much shorter time interval than what could have been achieved for advection-based tracer penetration from the cortical surface. However, Xie et al. (22) show that a substantial part of the tracer (administered intrathecally) first travels along vessels before it starts penetrating laterally into the interstitial space. Although this could explain the short timescale for tracer penetration seen in Xie et al. (22), Figs. 3–5 show that interstitial diffusion predominates over interstitial advection, also when the tracer originates from paravascular spaces. We find that diffusion is compatible with the timescale seen in the tracer experiments in Xie et al. (22) (Fig. 4), and the estimated permeabilities were too low to allow for any significant advection. Even when we simulated flow and permeabilities for subvolumes with a much larger extracellular volume fraction than would be realistic for any physiological situation, we still estimated permeabilities incompatible with tracer velocities from Xie et al. (22) (subvolumes with extracellular volume fractions of 27.9% and 32.1% gave permeabilities of 33 $nm^2$ and 70 $nm^2$, respectively). Table 1 shows that our estimated permeabilities are about two orders of magnitudes lower than what is typically found in the literature.

**Advection versus Diffusion.** Using the above estimated permeabilities we found that the bulk flow velocities are low also when we assume an arterial source and a venous sink. In this model the vessels are assumed to be surrounded by a medium with homogeneous permeability and an extracellular volume fraction of 20%. Fig. 3 shows that except for the volume just outside the vessels, where the pressure gradient is steepest, the flow velocities would typically be less than 10 nm/s for our assumed pressure differences of 1 mmHg/mm, even for the permeability value from the geometry with the higher permeability.

The typical timescale for diffusion is much smaller than the timescale for advection and comparable to typical timescales seen in tracer recordings (Fig. 4). Fig. 4 shows clearance of an interstitial solute; i.e., we assume the concentration to be higher inside the parenchyma than at the pial surface or within the paravascular spaces. For concentration gradients in the opposite direction, as after intrathecal tracer infusion, the $y$ axes would be symmetrically inverted.

In Fig. 4 *A* and *B*, we show the concentration profile of different substances at three time instances after we decrease the concentration by $\Delta c$ at the boundary, which is either the paravascular space (Fig. 4*A*) or the pial surface (Fig. 4*B*). The light substance (green) with an effective diffusion constant corresponding to ions such as potassium, shows a prominent decay already after 5 s (dotted line), even at distances as far as 100 μm from the vessel (Fig. 4*A*) or the cortical surface (Fig. 4*B*). For larger solutes diffusion takes a much longer time. The red lines correspond to effective diffusion constants for 3 kDa Texas Red Dextran and the blue lines correspond to 70 kDa Dextran. However, even for 70 kDa Dextran the concentration is seen to be substantially reduced at a timescale of minutes, both around vessels (Fig. 4*A*) and as a function of distance from the cortical surface (Fig. 4*B*).

Diffusion is seen to reduce the concentration at a distance 100 μm from a vessel (Fig. 4*C*) and 100 μm from the cortical surface (Fig. 4*D*) substantially within 1 h, even for the very heavy 70 kDa Dextran. Note that here we have assumed efflux only

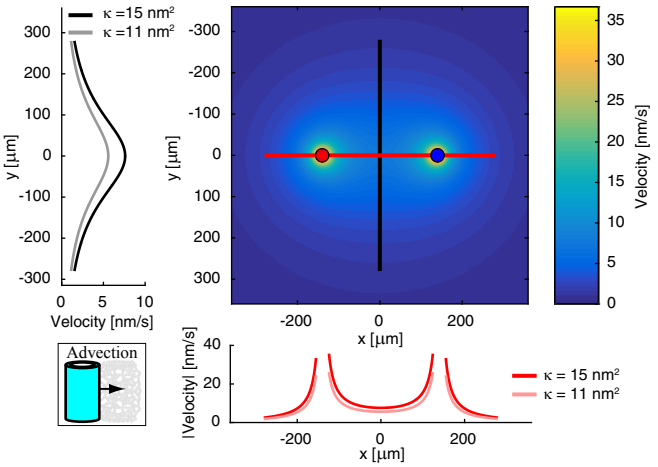


**Fig. 3.** Color plot showing velocity for the bulk flow from arteriole (red, solid circle) to venule (blue, solid circle) for the highest permeability $\kappa = 14.69\ nm^2$, assumed viscosity $\mu = 0.8$ mPa·s, and extracellular volume fraction of 20%. Diameter is 30 μm for both arteriole and venule, and their center-to-center distance is 280 μm (6, 28). The line plots in red/pink and black/gray correspond to the absolute value of the velocity profiles along the red ($x$ axis) and black ($y$ axis) lines in the color plot, and the two colors correspond to the two different permeabilities derived from the geometries with high tunnel volume fraction and low tunnel fraction. The pressure difference between the two vessel surfaces facing each other is 1 mmHg/mm. *Lower Left Inset* illustrates the cylindrical geometry of the vessels.

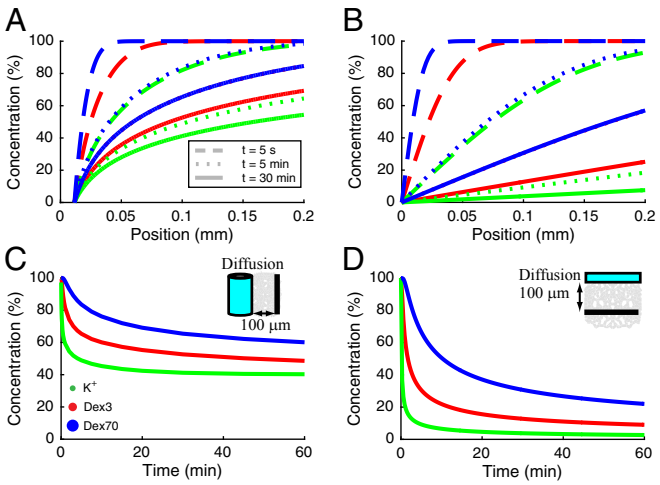


**Fig. 4.** (*A–D*) Diffusion from neuropil toward (*A* and *C*) a cylindrical vessel (*C*, *Inset*) and toward (*B* and *D*) the cortical surface (*D*, *Inset*). At time $t = 0$ the solute is assumed to be evenly spread throughout the interstitial space, and the cortical surface/cylinder is assumed to have zero concentration of the solute. The different colors correspond to effective diffusion coefficients for potassium ions (green), 3 kDa Texas Red Dextran (red), and 70 kDa dextran (blue). (*A*) Concentration profile around a vessel for three time instances. (*B*) Concentration profile below the cortical surface for three time instances. (*C*) Concentration of the three solutes as a function of time at a distance 100 μm from the cylinder center. (*D*) Concentration of the three solutes as a function of time 100 μm below the cortical surface.

from one vessel. If more vessels were assumed, the concentrations would have been decreased substantially in Fig. 4 *A* and *C*.

A more direct way to compare advection to diffusion is to compare the size of the advection term to the size of the diffusion term in the diffusion–convection equation by use of the Péclet number (Pe), $\mathrm{Pe} = Lv/D^*$. This number is plotted for a series of solutes of different sizes in Fig. 5. $L$ is the typical size of the system, here taken to be the average distance between the surfaces of an arteriole–venule pair (238 μm); $v = 12.2$ nm/s is the advection velocity, here taken to be the average velocity for the geometry with the highest permeability; and $D^*$ is the effective diffusion constant of the different solutes in brain tissue. For $\mathrm{Pe} \ll 1$ diffusion predominates, and in Fig. 5 we see that even for the most heavy solutes, such as 70 kDa Dextran and ovalbumin, the Péclet number is substantially lower than one for the assumed pressure gradient of 1 mmHg/mm. Hence, diffusion predominates over advection, even for large molecules. For illustrational purposes we have added a pressure gradient of 2 mmHg/mm in Fig. 5. Even for this pressure gradient most solutes have Péclet numbers well below one, although 70 kDa Dextran is seen to be approaching one (0.69).

## Discussion

Surprisingly little is known about the mechanisms that govern the movement of molecules between brain cells. As the brain interstitial space is particularly narrow and tortuous, the complexity of this space has so far defied any attempts to realistically simulate solute movement within it. New opportunities for such simulations arose with the recent generation of 3D representations that faithfully describe the interstitial space (18). Here we take advantage of these representations—and of recent developments in computer hardware, processing power, and software tools—to show that interstitial permeability is much lower and solute movement is much more constrained than previously assumed. Movement occurs by diffusion rather than being driven by bulk flow. This conclusion holds even in simulations with an abnormally high extracellular volume fraction (32.1%).

The existence of a bulk flow of interstitial fluid has been debated for decades. Syková and Nicholson (19) concluded that such flow is restricted to the paravascular spaces rather than taking place throughout the extracellular space. However, on introducing the glymphatic concept Nedergaard and coworkers (10) expressed the view that waste products are cleared by bulk flow through the interstitium. The present data compel us to revise the concept of the glymphatic system. The key idea embedded in the term glymphatic is that waste is cleared from the brain by a glia-dependent mechanism, analogous to the lymphatic system in other organs (29, 30). The critical experiment in support of this concept showed that amyloid $\beta$ and other compounds were cleared less efficiently in AQP4-deficient mice than in wild type (10). AQP4 is strongly expressed in glia, more specifically in the astrocytic endfeet that surround brain vessels (31). In terms of involvement of glia in waste removal the glymphatic concept is not challenged by our results. However, according to the glymphatic concept as originally described, paraarterial and paravenous spaces connect through convective flow in the neuropil. Our findings strongly suggest that this is untenable and that diffusion prevails in the interstitial space.

The present findings have pronounced implications for future research. The idea of there being an advection in the interstitial space directed attention to mechanisms underlying the control of extracellular volume and hydrostatic pressure gradients within brain tissue. On the other hand, if diffusion predominates—as the present data suggest—future research efforts should aim at understanding how concentration gradients are established and maintained. Attention should then be directed to transport processes at the brain–blood interface and to the nature and scale of advection along brain vessels. Paravascular advection is required to effectively maintain the concentration gradients that are prerequisites for diffusion through neuropil. AQP4 could facilitate paravascular advection, which in turn could explain why appropriate clearance may depend on the presence of this water channel.

The major premise for our conclusion is that the permeability of the interstitial space is so low that it effectively precludes advection through brain neuropil at realistic pressure gradients. The question is why our permeability estimates differ by order of magnitudes from those of previous studies. The other high permeabilities reported in Table 1 are either based on simultaneous fluid infusion and pressure recordings (5, 23–27) or simulated by the use of simplified geometries (6). Combined infusion and pressure recordings may lead to overestimated permeabilities due to tissue displacement and because fluid is escaping along high-permeability paths such as the paravascular spaces. Simulations are, on the other hand, critically dependent

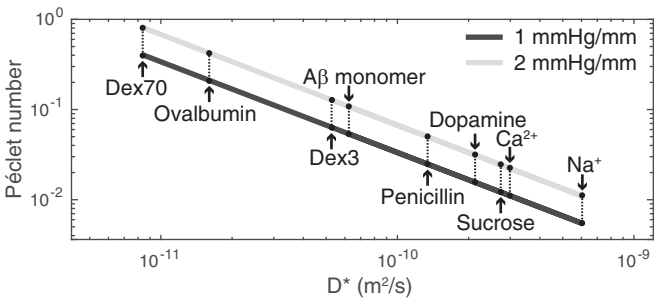


**Fig. 5.** Péclet numbers. Shown are effective diffusion coefficients ($D^*$) from Syková and Nicholson (19).

**Table 1. Comparison of permeabilities from the literature**

| Permeability, $nm^2$ | Source |
|---|---|
| 10–20 | This study, geometry from ref. 18 |
| 1,280 | Ref. 23, estimated from ref. 24 |
| 2,480 | Ref. 23, estimated from ref. 25 |
| 1,360 | Ref. 23, estimated from ref. 26 |
| 720 | (6) |
| 4,000 | (27) |
| 1,600 | (5) |

A viscosity of 0.8 mPa·s was assumed when the permeability was converted from hydraulic conductance.

on the right dimensions of the interstitial space. For a given extracellular volume fraction the dimension of the extracellular space is a function of the obstacle size. The 3D reconstructions used in our simulations indicate a mean obstacle size of far less than 1 μm, and we end up with a relatively low permeability. By comparison, Jin et al. (6) assume an extracellular volume fraction similar to what is used here (20%), but their simulations are based on artificially created 2D obstacles with a much larger mean obstacle size of 5 μm, and they arrive at a much larger permeability. However, even with such a large obstacle size they end up with a conclusion that is in line with ours: Diffusion predominates when it comes to solute movement through the extracellular space. The same conclusion is also reached by Asgari et al. (5), using a simplified model. We show that this conclusion holds in a realistic 3D model and even for very large molecules such as ovalbumin.

As stated above, our simulation precludes advection through brain neuropil at realistic pressure gradients. What are realistic pressure gradients in this context? Through a cardiac cycle the peak-to-peak intracranial pressure amounts to less than 10 mmHg. However, the pulsatility is almost synchronous throughout the brain, and the minute differences seen in simultaneous recordings of intracranial pressures give rise to much smaller pressure gradients than the $1\ \mathrm{mmHg/mm}$ assumed here (32). Pressure gradients within the brain and/or CSF are typically reported to be less than $0.01\ \mathrm{mmHg/mm}$ (32, 33). Thus, our assumption that these gradients are $1\ \mathrm{mmHg/mm}$ should be seen as an upper estimate. Unfortunately, technologies are not available for direct measurements of pressure gradients between neighboring brain vessels, i.e., those gradients that drive advection, if any, through brain neuropil.

We conclude that diffusion through interstitial space combined with paravascular advection substitutes for the lymphatic drainage system in other organs. This has profound implications for our understanding of how waste products are cleared from brain and of how drugs, nutrients, and signal molecules permeate brain neuropil.

## Methods

**Finite-Element Simulations.** ISF is assumed to be incompressible Newtonian fluid, and the flow is modeled by the Stokes equations $\mu\nabla^2\mathbf{v} + \nabla p = \mathbf{0}$ and $\nabla \cdot \mathbf{v} = \mathbf{0}$. Here $\mathbf{v}$ is velocity vector and $p$ the pressure within ISF. The viscosity $\mu$ of the ISF is assumed to be 0.8 mPa·s. As we use linear elements for both velocity and pressure, a stabilization term $0.2\,h^2\nabla^2 p$ is added to the second equation (34), with $h$ denoting the element size. To drive flow, a pressure gradient of 1 mmHg/mm is applied in one direction. This is enforced as a Neumann boundary condition, i.e., constant pressure at the inflow and outflow surfaces. On the remaining exterior boundary we used a symmetry assumption ($\mathbf{v} \cdot \mathbf{n}_\perp = 0$, where $\mathbf{n}_\perp$ is the unit normal vector for the outer surface), and at the interior cell surface boundaries we use the no-slip condition, $\mathbf{v} = 0$.

The resulting partial differential equations are solved in FEniCS (20). Postprocessing of the data, including computation of total flux and visualization, was carried out using Paraview (35).

The meshes on which the computations are performed are generated using the CGAL backend of FEniCS' mesh generation submodule mshr. For the largest simulation the mesh consisted of 84 million tetrahedrons and more than 1,000 CPU hours were needed to simulate the flow (279 min on 224 Intel E5-2670 processors).

A highly detailed mesh is required to adequately resolve the intricate geometry of the interstitial space. To test whether the mesh is sufficiently fine, the ideal test would be to refine it once, repeat all computations, and check that the results do not significantly change. However, because the number of mesh elements is already very large, this is not computationally feasible.

Instead we used a less strict test. For both geometries we performed the simulation on a smaller volume measuring 0.52 μm × 0.52 μm × 0.45 μm. For the default simulation we found the baseline permeability for these subvolumes by applying a mesh size similar to what was used in the full simulations. We then refined the mesh by increasing the number of tetrahedrons 7 times. After three refinements (resulting in a total of 343 times as many volume elements as the original mesh) we reached the upper limit for what was computationally feasible. For the reduced geometry with a high tunnel fraction (Fig. 1*D*) the extracellular volume fraction was 32.1% and refinements gave the following permeability series for the subvolume, listed from the default value to the most refined value: 54.26 $nm^2$, 61.91 $nm^2$, 65.59 $nm^2$, and 67.74 $nm^2$. For the reduced geometry with a low tunnel fraction (Fig. 1*C*) the extracellular volume fraction was 27.9% and the corresponding series was 25.22 $nm^2$, 29.49 $nm^2$, 31.24 $nm^2$, and 32.14 $nm^2$. These trends predict that the series should converge for about 70 $nm^2$ and 33 $nm^2$, respectively. This is seen by fitting each series to a permeability model $\kappa = \kappa_\infty - a/(x - b)$, where $\kappa_\infty$ is the asymptotic permeability for small mesh sizes, and $x$ is the reciprocal of the mesh size. As the volumes of the tetrahedrons are reduced by 7 times for each refinement, the typical mesh size is correspondingly reduced by $7^{1/3} \approx 1.9$ times. Thus, $x = x_j = 7^{j/3}$ denotes the $x$ values fitted for $j = 0, 1, 2, 3$, with corresponding permeabilities $\kappa_j$ at the $y$ axes. $\kappa_\infty$, $a$, and $b$ are parameters fitted in the model. A nonlinear least-squares fit gives the asymptotic permeabilities 69.8 $nm^2$ and 33.0 $nm^2$, corresponding to a 28.7% and a 30.8% increase from the baseline permeabilities, respectively. When the mesh size becomes infinitesimally small, we therefore expect the permeabilities to increase by about 30% also for the full geometries.

**Interstitial Flow from Arteriole to Venule.** The interstitial flow velocities for the arteriole–venule geometry plotted in Fig. 3 were found analytically (*SI Interstitial Flow from Arteriole to Venule*).

**Diffusion from the Cortical Surface.** If we assume the cortical surface to be perfectly planar and the lateral concentration to be constant, the one-dimensional diffusion equation describes the system. A constant concentration $c(z, t) = c_0$ at time $t < 0$ followed by an abrupt decrease in concentration at the boundary (cortical surface), $c(z = 0, t \geq 0) = 0$, has the solution $c(z, t) = c_0\ \mathrm{erf}(z/\sqrt{4D^* t})$, where erf($x$) is the SE function, $z$ is distance from the cortical surface, and $D^*$ is the effective diffusion coefficient.

**Diffusion from the Paravascular Space.** The diffusion equation was solved in polar coordinates with a commercial software package (MATLAB 8.6, R2015b; The MathWorks Inc.). The outer surface of the paravascular space was assumed to have the shape of an infinitely long cylinder with an outer radius $a$, and the solute was allowed to diffuse throughout the interstitial space defined by $a < r < R$. Similarly to the planar diffusion, a constant concentration $c(r, t) = c_0$ was assumed at time $t < 0$ followed by an abrupt decrease in concentration at the boundary (paravascular space), $c(r = a, t \geq 0) = 0$. The concentration was kept constant at the distal boundary $c(r = R, t > 0) = c_0$, where $R$ is much larger than the distances plotted in Fig. 4 ($R \gg 0.2$ mm).

**ACKNOWLEDGMENTS.** This work was funded by the Research Council of Norway (Grants 226696 and 240476); the European Union's Seventh Framework Program for research, technological development, and demonstration under Grant 601055; the Molecular Life Science Initiative at the University of Oslo, Simula-University of California, San Diego-University of Oslo Research and PhD training program; and the Letten Foundation. The simulations were run on the Abel Cluster (Project NN9279 K), owned by the University of Oslo and the Norwegian Metacenter for High-Performance Computing and operated by the Department for Research Computing at University Center for Information Technology, the University of Oslo Technical Department, www.hpc.uio.no/. An approximate total of 60,000 CPU hours were spent on the simulations for this study.

1. Louveau A, et al. (2015) Structural and functional features of central nervous system lymphatic vessels. *Nature* 523:337–341.
2. Aspelund A, et al. (2015) A dural lymphatic vascular system that drains brain interstitial fluid and macromolecules. *J Exp Med* 212:991–999.
3. Smith AJ, Jin BJ, Verkman AS (2015) Muddying the water in brain edema? *Trends Neurosci* 38:331–332.
4. Thrane AS, Rangroo Thrane V, Plog BA, Nedergaard M (2015) Filtering the muddied waters of brain edema. *Trends Neurosci* 38:333–335.
5. Asgari M, de Zélicourt D, Kurtcuoglu V (2016) Glymphatic solute transport does not require bulk flow. *Sci Rep* 6:38635.
6. Jin BJ, Smith AJ, Verkman AS (2016) Spatial model of convective solute transport in brain extracellular space does not support a "glymphatic" mechanism. *J Gen Physiol* 148:489–501.
7. Abbott NJ (2004) Evidence for bulk flow of brain interstitial fluid: Significance for physiology and pathology. *Neurochem Int* 45:545–552.
8. Hladky SB, Barrand MA (2014) Mechanisms of fluid movement into, through and out of the brain: Evaluation of the evidence. *Fluids Barriers CNS* 11:26.
9. Louveau A, Da Mesquita S, Kipnis J (2016) Lymphatics in neurological disorders: A neuro-lympho-vascular component of multiple sclerosis and Alzheimer's disease? *Neuron* 91:957–973.
10. Iliff JJ, et al. (2012) A paravascular pathway facilitates CSF flow through the brain parenchyma and the clearance of interstitial solutes, including amyloid $\beta$. *Sci Transl Med* 4:147.
11. Iliff JJ, et al. (2013) Cerebral arterial pulsation drives paravascular CSF-interstitial fluid exchange in the murine brain. *J Neurosci* 33:18190–18199.
12. Kiviniemi V, et al. (2016) Ultra-fast magnetic resonance encephalography of physiological brain activity - Glymphatic pulsation mechanisms? *J Cerebr Blood Flow Metabol* 36:1033–1045.
13. Cserr HF, Ostrach LH (1974) Bulk flow of interstitial fluid after intracranial injection of blue dextran 2000. *Exp Neurol* 45:50–60.
14. Rennels ML, Gregory TF, Blaumanis OR, Fujimoto K, Grady PA (1985) Evidence for a 'paravascular' fluid circulation in the mammalian central nervous system, provided by the rapid distribution of tracer protein throughout the brain from the subarachnoid space. *Brain Res* 326:47–63.
15. Tarasoff-Conway JM, et al. (2015) Clearance systems in the brain-implications for Alzheimer disease. *Nat Rev Neurol* 11:457–470.
16. Carare RO, et al. (2008) Solutes, but not cells, drain from the brain parenchyma along basement membranes of capillaries and arteries: Significance for cerebral amyloid angiopathy and neuroimmunology. *Neuropathol Appl Neurobiol* 34:131–144.
17. Morris AWJ, et al. (2016) Vascular basement membranes as pathways for the passage of fluid into and out of the brain. *Acta Neuropathol* 131:725–736.
18. Kinney JP, et al. (2012) Extracellular sheets and tunnels modulate glutamate diffusion in hippocampal neuropil. *J Comp Neurol* 521:448–464.
19. Syková E, Nicholson C (2008) Diffusion in brain extracellular space. *Physiol Rev* 88:1277–1340.
20. Logg A, Mardal KA, Wells G (2012) *Automated Solution of Differential Equations by the Finite Element Method: The FEniCS Book*, Lecture Notes in Computational Science and Engineering, eds Logg A, Mardal KA, Wells G (Springer, Berlin), Vol 84.
21. Halnes G, Østby I, Pettersen KH, Omholt SW, Einevoll GT (2013) Electrodiffusive model for astrocytic and neuronal ion concentration dynamics. *PLoS Comput Biol* 9:e1003386.
22. Xie L, et al. (2013) Sleep drives metabolite clearance from the adult brain. *Science* 342:373–377.
23. Smith JH, Humphrey JAC (2007) Interstitial transport and transvascular fluid exchange during infusion into brain and tumor tissue. *Microvasc Res* 73:58–73.
24. Morrison PF, Laske DW, Bobo H, Oldfield EH, Dedrick RL (1994) High-flow microinfusion: Tissue penetration and pharmacodynamics. *Am J Physiol* 266:R292–R305.
25. Bobo RH, et al. (1994) Convection-enhanced delivery of macromolecules in the brain. *Proc Natl Acad Sci USA* 91:2076–2080.
26. Prabhu SS, et al. (1998) Distribution of macromolecular dyes in brain using positive pressure infusion: A model for direct controlled delivery of therapeutic agents. *Surg Neurol* 50:367–375.
27. Basser PJ (1992) Interstitial pressure, volume, and flow during infusion into brain tissue. *Microvasc Res* 44:143–165.
28. Adams DL, Piserchia V, Economides JR, Horton JC (2015) Vascular supply of the cerebral cortex is specialized for cell layers but not columns. *Cerebr Cortex* 25: 3673–3681.
29. Nedergaard M (2013) Garbage truck of the brain. *Science* 340:1529–1530.
30. Nagelhus EA, Ottersen OP (2013) Physiological roles of aquaporin-4 in brain. *Physiol Rev* 93:1543–1562.
31. Nielsen S, et al. (1997) Specialized membrane domains for water transport in glial cells: High-resolution immunogold cytochemistry of aquaporin-4 in rat brain. *J Neurosci* 17:171–180.
32. Eide PK, Sæhle T (2010) Is ventriculomegaly in idiopathic normal pressure hydrocephalus associated with a transmantle gradient in pulsatile intracranial pressure? *Acta Neurochir* 152:989–995.
33. Alperin NJ, Lee SH, Loth F, Raksin PB, Lichtor T (2000) Mr-intracranial pressure (ICP): A method to measure intracranial elastance and pressure noninvasively by means of MR imaging: Baboon and human study. *Radiology* 217:877–885.
34. Hughes TJR, Franca LP, Balestra M (1986) A new finite element formulation for computational fluid dynamics: V. Circumventing the Babuška-Brezzi condition: A stable Petrov-Galerkin formulation of the Stokes problem accommodating equal-order interpolations. *Comput Methods Appl Mech Eng* 59:85–99.
35. Ahrens J, Geveci B, Law C (2005) ParaView: An end-user tool for large data visualization. *Visualization Handbook*, eds Hansen CD, Johnson CR (Elsevier Butterworth-Heinemann, Burlington, MA), pp 717–731.